EIR-Bericht Nr. 598
Juli 1986

EIR-Bericht Nr. 598

Juli 1986

Recent R+D Contributions in the Field of Fast Reactor Safety

P. Wydler (Editor)

Contributors:

T.V. Dury, P. Dutton (Dounreay NPDE, Scotland),
W. Heer, M. Hudina, C. Inversini, J.F. Jaeger, D. Jakeman,
B. Sigg (ETHZ, Zürich), B.L. Smith, T.v. Weissenfluh,
H.U. Wenger, P. Wydler

Eidgenössisches Institut für Reaktorforschung
Institut Fédéral de Recherches en Matière de Réacteurs
Swiss Federal Institute for Reactor Research

CH-5303 Würenlingen Tel. 056 99 21 11 Telex 82 7417 eir ch

EIR Report No. 598

RECENT R+D CONTRIBUTIONS IN THE FIELD OF FAST REACTOR SAFETY

Papers presented at BNES Conference on
the Science and Technology of Fast Reactor Safety, Guernsey, 1986

P. Wydler (Editor)

Contributors:

T.V. Dury, P. Dutton*, W. Heer, M. Hudina, C. Inversini, J.F. Jaeger,
D. Jakeman**, B. Sigg***, B.L. Smith, T. v. Weissenfluh, H.U. Wenger, P. Wydler

Würenlingen, July 1986

*Dounreay Nuclear Power Development Establishment, Scotland
**now at AEE Winfrith, Dorchester, Dorset, England
***Nuclear Engineering Laboratory, ETHZ, Zürich

PREFACE

Activities in the framework of EIR's Fast Reactor Safety Project currently concentrate on two themes, decay heat removal by natural convection and HCDA induced fluid-structure interaction. In addition, some recently completed work relating to fuel coolant interaction is worth mentioning. The three EIR papers presented at the BNES Conference on the Science and Technology of Fast Reactor Safety, Guernsey, 1986, conveniently summarise activities and are therefore used to compile this EIR Report.

Guernsey paper no. 536 describes natural convection studies carried out on a sodium-cooled 37-pin test section. The aim of the studies is to improve the understanding of natural convection effects in subassemblies subjected to loss-of-flow conditions as may arise, for instance, from an inlet blockage. The work is complementary to similar work in other countries and has led to an interesting information exchange, particularly with groups in France and the United Kingdom.

In the framework of an agreement with Euratom and the UKAEA, EIR contributes to the development and validation of the containment code SEURBNUK/EURDYN. In addition, EIR collaborates with the CEA on a code intercomparison and validation exercise based on the MARA experiments, a series of 1/30th scale containment tests performed at Cadarache. Guernsey paper no. 501 deals with an application of SEURBNUK/EURDYN and describes how the code can be used, together with a general purpose structural mechanics code, to assess the fluid-structure interaction during sodium impact for a realistic (i.e. three-dimensional) reactor cover.

The last paper, no. 591, reports results from a series of small scale Freon-water experiments to simulate fuel coolant interaction effects. Although limited in scope, the work merits attention since it provides alternative explanations for pressures observed during fuel coolant interaction events and hence may influence future FCI modelling.

CONTENTS

Studies of decay heat removal by natural convection using the SONACO sodium-cooled 37-pin bundle

P. WYDLER, T.V. DURY, M. HUDINA, T. v.WEISSENFLUH
Federal Institute for Reactor Research, Würenlingen, Switzerland

B. SIGG
Nuclear Engineering Laboratory, ETHZ, Zürich, Switzerland

F. DUTTON
Dounreay Nuclear Power Development Establishment, Scotland

Natural convection measurements in an electrically heated sodium-cooled rod bundle are being performed with the aim of contributing to a better understanding of natural convection effects in subassemblies with stagnant sodium and providing data for code validation. Measurements include temperature distributions in the bundle for different cooling configurations which simulate heat transfer to the intersubassembly gap and neighbouring subassemblies and possible thermosyphonic interaction between a subassembly and the reactor plenum above. Conditions for which stable natural convection patterns exist are identified, and results are compared with predictions of different computer codes of the porous-medium type.

INTRODUCTION

1. Heat transfer by natural convection plays an important role in the safety analysis of LMFBR's and, more recently, has become a favoured design feature to increase the reliability of decay heat removal systems. Analytical tools for predicting and analysing natural convection flows in complex geometries are now available, but still require further validation and improvement. The objectives of the SONACO (sodium natural convection) experiment in an electrically heated rod bundle are (1) to contribute to a better understanding of the basic thermohydraulic phenomena in subassemblies with recirculating flows within the bundle, and (2) to provide data for code validation.

2. Recirculation within a subassembly occurs for small or vanishing net coolant flows. In the situation of a subassembly inlet blockage, recirculation enhances the transfer of decay heat to the intersubassembly gap and neighbouring subassemblies and hence may prevent fuel melting. A different situation arises in some accidental transients in which flow stagnation in the whole core may occur, at least temporarily (e.g. before natural circulation in the primary circuit has fully developed). In the latter case, and for subassemblies with sufficiently small flow restriction at the outlet, Webster (ref. 1) has predicted thermosyphonic interaction between the subassemblies and the reactor plenum above. SONACO allows the effects of natural convection in a rod bundle to be investigated, for both the "blocked subassembly" and the "pure thermosyphon" situation, as well as for other more complicated situations.

THE SONACO EXPERIMENT

Experimental arrangement

3. The main features of the SONACO experiment are illustrated in Fig. 1. Table 1 gives basic bundle parameters, including a comparison with actual reactor parameters. Rod diameter and pitch-to-diameter ratio are typical for fuel pins, but overall bundle dimensions are reduced by a factor of approximately 2. The electrically heated rods have a flat axial power profile and each rod can be connected to one of three power supplies, permitting the simulation of power tilts. Currently, total power is limited to 30 kW due to restrictions in cooling capacity. The rods are positioned on a hexagonal pitch by means of honeycomb grid spacers with an axial separation of 200 mm, and the bundle is surrounded by two concentric hexcans with a 3.8 mm gap between them. Thermal insulation with embedded guard heaters ensures an adiabatic boundary condition at the surface of the outer hexcan.

Table 1. Principal design parameters of SONACO and typical fuel subassemblies

Parameter	SONACO	PFR	Super Phenix
Rod diameter	8.6 mm	5.84 mm	8.5 mm
Ratio pitch to diameter	1.27	1.27	1.14
No. of rods	37	325	271
Heated or fiss. length	500 mm	914 mm	1000 mm
Rod surface flux	6.0 W/cm^2 (30 kW)	7.4 W/cm^2 (5% power)	5.2 W/cm^2 (5% power)
Max. sodium temperature	400°C	690°C	700°C

4. Heat can be removed by sodium coolant passing through either the gap between the hexcans or a cooling coil in the plenum above the bundle. If desired, these (radial and axial) cooling modes can be combined and a small amount of forced flow in the bundle can be

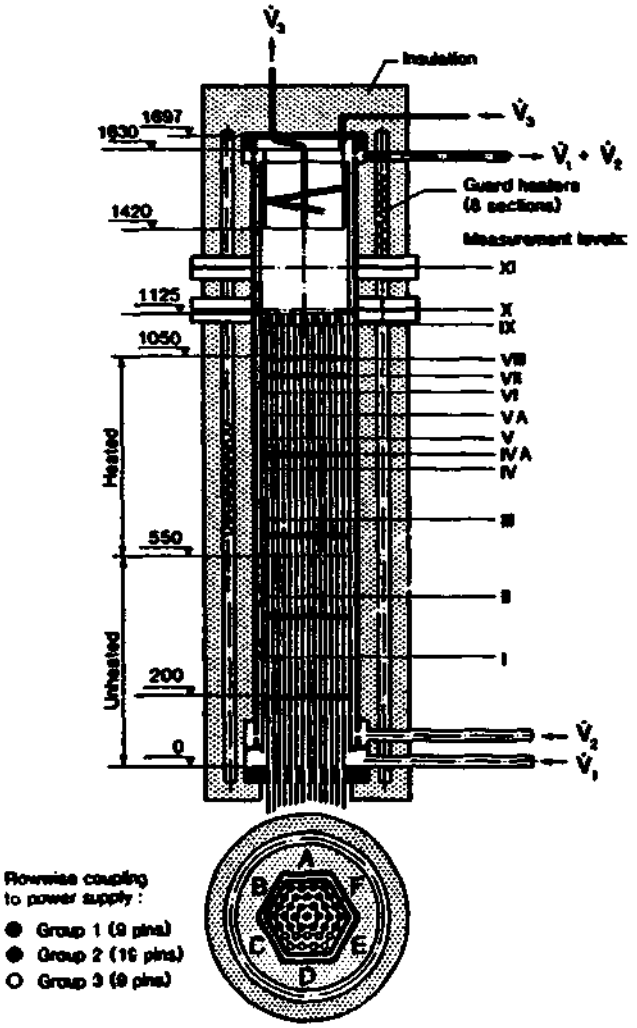

Fig. 1. Design of the SONACO test section

superimposed. The combined radial and axial cooling capability is a unique feature of the SONACO experiment and is expected to provide otherwise unobtainable information on the stability of natural convection flows.

Instrumentation

5. The instrumentation of the SONACO test section consists mainly of thermocouples placed at 10 different levels (labelled I to VIII in Fig. 1) in the heater rods and on both surfaces of the hexcans. Ninety-six thermocouples in the rods allow axial and radial temperature profiles to be measured with good spatial resolution. Other thermocouples in the hexagonal gap, the cooling coil and the thermal insulation provide additional information which is required, for instance, for checking the total heat balance.

6. Local fluid velocities are measured using permanent-magnetic transducers based on the Faraday effect (ref. 2). Five of these transducers (incorporated in heater rods at level IX) detect subchannel velocities and four mobile transducers (at levels X and XI) permit recording of velocity profiles in the upper plenum. Although in pure natural convection regimes the transducers operate at the limit of their sensitivity, the measurement technique has provided first direct proof of the existence of a recirculation loop near the bundle exit.

Status of programme and future outlook

7. The SONACO experiment is being performed by EIR (the Swiss Federal Institute for Reactor Research) with the support of the Nuclear Engineering Laboratory from the Federal Institute of Technology at Zürich. The Centre d'Etudes Nucléaires de Grenoble and the Nuclear Power Development Establishment Dounreay participate in the analysis of the data. A first phase of the programme (Phase 1A), concentrating on the radial cooling mode, was completed in 1985, and preliminary results have been published (ref. 3).

8. The present paper reports final Phase 1A results and first results for the axial cooling mode. The revised Phase 1A results take account of an independently determined value for the radial conductivity of the bundle (cf. par. 14). A summary of the experimental conditions for the cases discussed below is given in Table 2, including measured and predicted maximum temperature differences in the bundle.

9. A future phase of the experiment will investigate cooling with combined radial and axial heat removal, and it is planned to extend the measurements to higher temperatures with an aim to complement similar research work in other countries.

Table 2. Experimental conditions and comparison of measured and predicted temperature differences

SONACO test number	Flow (l/s)		T_{ref}	Total power	Power distribution (pin power ratio for groups 1, 2 and 3)	$T_{max} - T_{ref}$ (°C)		
	Annulus	Cooler	(°C)	(kW)		Measured	BACCHUS-T	INCA
1115	0.991	-	250.7	9.9	uniform	60	56	57
1125	0.244	-	242.0	10.1	uniform	79	76	77
1130	0.123	-	235.4	10.1	uniform	105	105	104
1136	0.241	-	217.8	19.6	uniform	143	141	138
1159	0.247	-	217.6	29.4	uniform	202	202	196
ACU001	-	0.10	194.3	2.5	uniform	not given for axially cooled cases because of temperature fluctuations		
ACT012	-	0.10	158.9	2.5	2 : 1.5 : 1			
ACT002	-	0.10	162.9	5.0	2 : 1.5 : 1			

T_{max}: Maximum temperature in bundle, T_{ref}: Annulus or axial cooler inlet temperature

COMPUTER SIMULATIONS

Computer codes

10. Both computer codes used to simulate SONACO experiments use a "porous medium" representation of the rod bundle and sodium coolant, assuming spatial homogeneity of properties. BACCHUS-T (ref. 4) uses a two-dimensional, cylindrical-coordinate representation of the bundle and models it from the upper surface of the spacer grid below the beginning of heating up to the top of the rods. This upper boundary is assumed to be at constant and uniform pressure, but permeable to flow. The bottom and bundle centre-line boundaries are adiabatic, while the annulus and its coolant are defined in terms of entry temperature, flowrate and heat transfer coefficient from the bundle sodium. INCA (ref. 5) uses a three-dimensional model of the test-section, including upper plenum. The upper boundary is then adiabatic and impermeable, while the other boundary conditions are set in the same way as for BACCHUS-T.

11. Both codes incorporate an empirical grid spacer model, based on earlier EIR work, which defines overall non-recoverable pressure drop as a function of flowrate. No effect on heat transfer is included, but crossflow is prevented within the zone occupied by the spacer.

12. Axial centre-line temperatures for three different spacer situations and a (theoretical) no-gravity case are plotted in Fig. 2. The figure illustrates that the grid spacer model overpredicts the distorting effect on the profile, and gives a lower peak temperature than the standard wire spacer model of BACCHUS-T, because of the recirculation between the grid spacers. However, the lowest peak temperature would occur if all spacers were removed, since this enhances overall recirculation between bundle and plenum. The elimination of gravity, and hence of buoyancy forces and natural convection, results in considerably higher temperatures over the whole heated length of the bundle.

Heat conduction through rods

13. A particular problem in porous-medium calculations is the heat conduction through the rods. In the calculations, radial and axial conduction through the rods is not modelled explicitly, but taken into account by a conductivity enhancement factor (C.F.) for the coolant (The precise definition of this factor is related to the formulation of the conduction in terms of permeabilities and is code dependent). A parameter study for the radial cooling configuration of SONACO showed that the temperature profiles are rather sensitive to the conductivity factor (cf. Fig. 3).

14. Hence, the conductivity factor was determined carefully in two different ways. Firstly, the transverse conduction was calculated for a cylindrical approximation of a hexagonal rod cell. Secondly, the average radial conductivity of the bundle was derived from radial temperature distributions in a low power experiment with radial cooling, for which the convection in the bundle could be shown to be negligible. Although the accuracy of the analytical result is limited by uncertain contact resistances between the different rod materials and density variations in the boron nitride insulation, the calculated conductivity factor agreed well with the measured factor of 2.5. This value was therefore adopted in the final analysis of the results.

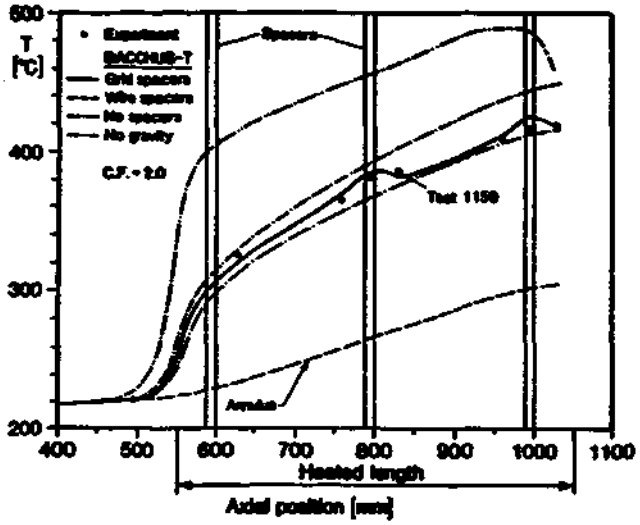

Fig. 2. Spacer and gravity parameter study

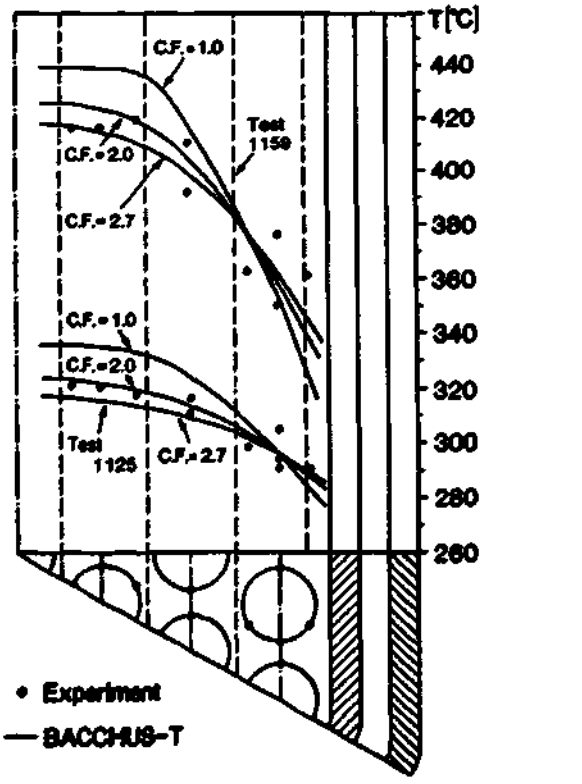

Fig. 3. Influence of conductivity factor

Modelling of the "thermosyphon" case

15. INCA calculations of the purely axial cooling mode use both 90° and 180° sector models of the test section, which impose four-fold and two-fold symmetry on the solutions, respectively. All boundaries are made adiabatic, and a linear coil temperature profile is prescribed, determined from the coil coolant flow and the total power. Free-slip boundary conditions are used in the plenum in conjunction with (rather arbitrary) enhancement factors of 100 on the viscosity, and 1 or 20 on the thermal conductivity, as approximate means of representing turbulent mixing.

16. An upper plenum and cooling coil model is currently being incorporated in BACCHUS-T and will also allow axially cooled experiments to be simulated. The model keeps within the confines of the existing code geometry, but is as yet untested.

RESULTS

Radial heat removal

17. For the uniformly heated bundle with radial heat removal, the effects of power level and annulus flowrate on natural convection have been investigated. The results plotted in Figs 4-7 are axial centre-line temperature profiles and radial distributions at level VII, where the highest temperatures occur. In the axial plots, calculated annulus temperatures signify averages over the whole cross-section, whereas experimental ones are mid-wall values taken at the inner wall of the outer hexcan. For the radial plots the thermocouple positions are superimposed onto a one-twelfth sector of the hexagon and then projected upon the mid-wall diagonal, as shown in Fig. 3. Different thermocouples projected onto the same position in the plots have different symbols. The temperatures obtained from INCA are values interpolated for the exact thermocouple positions from calculated 3-dimensional temperature distributions. BACCHUS calculations yield averaged values for hexagonal rings. All temperature data in the plots are differences relative to the annulus inlet temperature.

18. The spread of experimental results is only partly due to the projection method. Other sources are deviation from uniform heating and coolant flow, as well as geometric distortions. Measured temperatures within the bundle are taken underneath the cladding, whereas calculated temperatures refer to the sodium. Therefore, at a power of 10 kW measured values are about 1°C higher than those calculated.

19. The effect of power level for constant annulus flow is illustrated in Figs 4 and 5. With rising power the relative contribution of natural convection to the heat removal increases, and consequently temperatures do not rise linearly with power. The axial plots again show that the spacers slightly impede the cooling of the bundle (cf. par. 12). A comparison of experimental and calculated results indicates that INCA somewhat underestimates the spacer effect, whereas BACCHUS tends to overestimate it. However, the overall agreement between experiment and calculation is, for all distributions, very satisfactory.

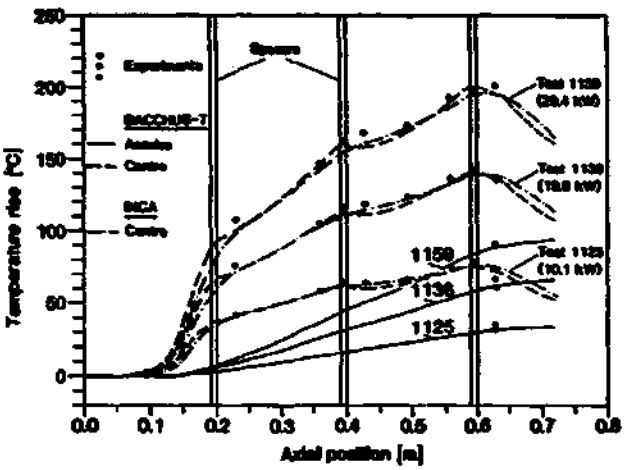

Fig. 4. Axial profiles for three power levels

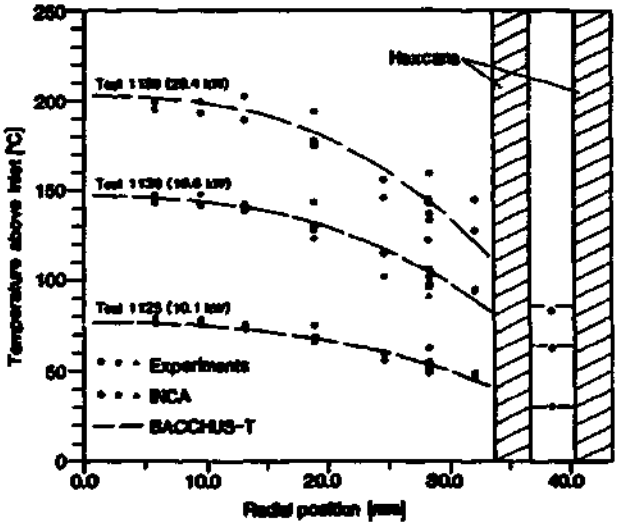

Fig. 5. Radial profiles for three power levels (axial level VII)

20. The effect of annulus flowrate for a fixed power of 10 kW is demonstrated in Figs 6 and 7. In addition to the obvious effect that the axial temperature rise must increase with decreasing annulus flow, the graphs indicate that the temperature difference between centre-line and annulus at levels in the upper part of the heated section is smaller for low flows through the annulus than for high ones. The main reason for this phenomenon seems to be the enhancement of convective enthalpy transport by a steeper axial temperature gradient (see also par. 22). The slightly larger disagreement between experiment and calculation for higher flow rates cannot be explained. A small systematic discrepancy between experimental and predicted annulus temperatures can be an effect of the difference in definition mentioned in par. 17 and a too-small heat transfer coefficient to the sodium flowing in the gap.

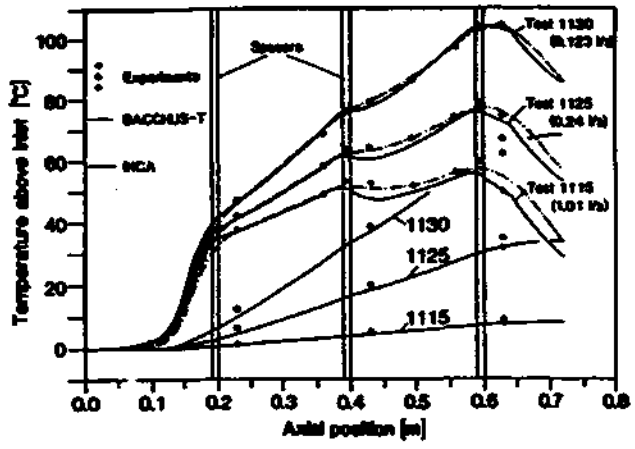

Fig. 6. Axial profiles for three lateral flows

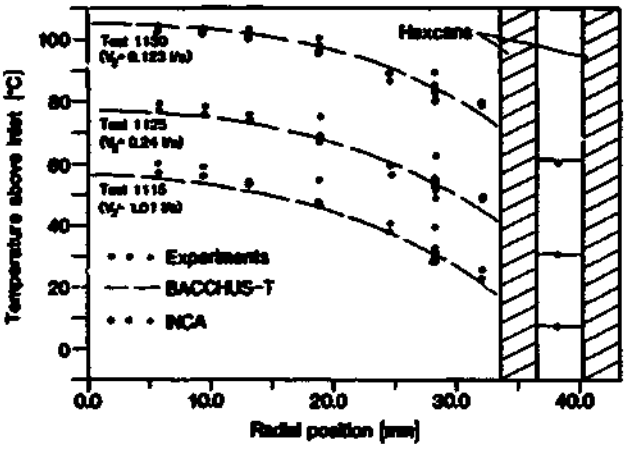

Fig. 7. Radial profiles for three lateral flows (axial level VII)

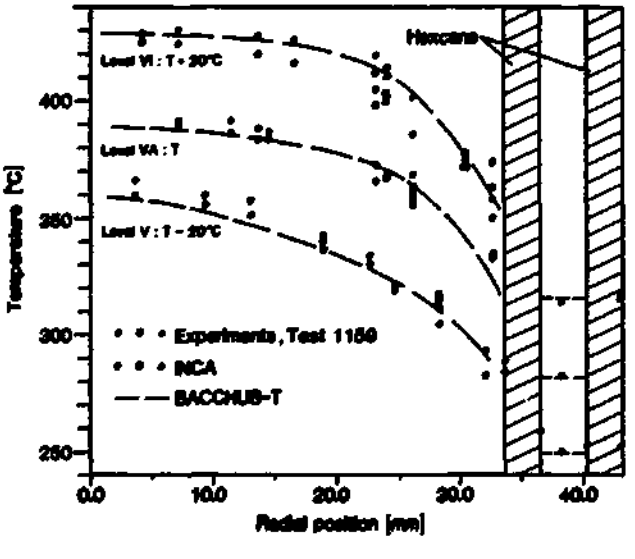

Fig. 8. Axial dependence of radial profiles

21. The influence of natural convection on heat transport makes itself felt by the non-linear temperature rise with power. Calculations show that, crudely speaking, two superimposed convection patterns are formed, an inter- and an intra-spacer flow field (ref. 3). The first transports hot sodium along the axis of the bundle upwards to the plenum, and colder fluid along the hexcan wall from the plenum down into the bundle. In addition, torus-shaped intra-grid eddies develop because of the higher flow resistance of the spacers. The sense of rotation is the same for both vortices. Therefore, the intra-grid vortex transports relatively hot sodium beneath a spacer level outwards to the hexcan and cooler sodium inwards above the next lower spacer.

22. Figure 8 shows radial temperature profiles for 3 different levels at a power of 30 kW. In order to eliminate interference between the data points of the three profiles, 20°C has been added to the temperatures at level VI and subtracted from those of level V. Experimental points and values calculated by INCA for the same positions are again distinguished by different symbols when lying on the same radial coordinate. However, the position of the thermocouples is not identical with that on level VII. The above-mentioned intra-grid eddy causes a flat radial temperature distribution at level VI because it supports radial heat flow, whereas at level V the temperature profile is steepened since the vortex counteracts the radial heat flow. The BACCHUS and INCA results shown in Fig. 8 agree fairly well with the experimental data. The discrepancies between experiment and INCA calculations seem to point to a slight underprediction of the intra-grid vortex by INCA, whereas the reasons for the differences between BACCHUS and experiment are more difficult to identify.

Axial heat removal

23. For the axial cooling configuration of SOMACO, preliminary measurements have been made at various powers, both with and without power tilts. Relatively large temperature fluctuations were observed in these measurements, and the temperatures were therefore recorded continuously over a period of 600 s, using a fast data acquisition system which samples every thermocouple once per second. Fig. 9 shows temperatures in the bundle relative to the inlet temperature of the cooling coil, the experimental points and, where indicated, error bars representing averages and 1σ standard deviations of the recorded data points, respectively.

24. The centre-line axial profile for a uniformly heated 2.5 kW case is shown at the bottom of the figure. A closer inspection of the basic data reveals that the transverse temperature profiles have an axially and azimuthally dependent tilt, and that temperature fluctuations are larger at the periphery than at the centre of the bundle - observations which are consistent with the assumption that the underlying natural convection modes are also time-dependent. An appropriate computer simulation, which has not yet been attempted, may thus require a full 360° representation of

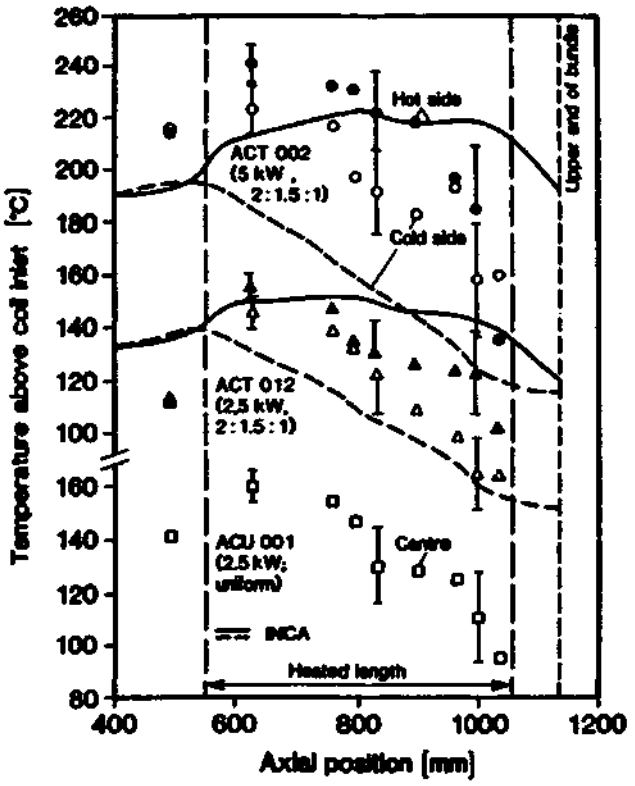

Fig. 9. Axial profiles for axial heat removal

the bundle and, possibly, a transient model. The centre-line axial profile was selected for Fig. 9, since this profile should be least influenced by azimuthal effects.

25. Also shown in the figure are temperature profiles at the hot and cold side of the bundle for 2.5 and 5 kW and a power tilt ratio of 2. In these cases the transverse temperature profiles appear to be consistent with the power tilt all along the heated section. As in the case with uniform heating, the fluctuations are smallest at the centre of the bundle, but, contrary to expectation, the fluctuations in the region of the peak temperature are not reduced noticeably by the overall recirculation which one would expect the power tilt to induce. The slight drop in average peak temperature caused by the power tilt is insignificant compared with the size of the fluctuations.

26. Since experiment has shown the axial cooling mode to be unstable, and it was expected that use of a power tilt might partially alleviate this, calculations have concentrated on cases with power tilts. Shown in Fig. 9 are INCA predictions using a 180° sector model and 20-fold plenum conductivity enhancement. Predictions without such enhancement are similar but lowered by approximately 25 and 40°C for the 2.5 and 5 kW cases, respectively. Clearly, the predicted (inverse) stratification is too small, especially on the hot side and at higher power. Whereas the maximum temperature is found near the bottom of the heated region, it is predicted at the grid in the centre of this region.

CONCLUSIONS

27. The SONACO experiment has proved to be a useful tool for basic studies of natural convection in subassembly geometry and for validating computer codes. Tests performed so far confirm the effectiveness of natural convection in removing heat from rod bundles with stagnant sodium.

28. In the radially cooled bundle, stable convection patterns develop and the temperature distributions are in overall good agreement with predictions based on the two porous-medium codes BACCHUS-T and INCA. A qualitative analysis of the measurements confirms the existence of vortices between the spacers, with the expected sense of rotation. The influence of spacers on natural convection is important, and the particular grid spacer model used gives satisfactory results, although some differences between BACCHUS-T and INCA in predicting the spacer effect are not yet fully understood.

29. For the simple thermosyphon with heat removal through the bundle outlet plenum up to the axial cooler, preliminary tests show large temperature fluctuations, and there appears to be no preferred convection pattern. When the symmetry is broken by a power tilt, a corresponding transverse temperature gradient develops but, for the moderate power tilts investigated, there is no clear indication of improved stability. First INCA predictions for the power tilt underestimated temperatures in the bundle, but with a model with artificially enhanced conduction in the plenum the results become more satisfactory.

30. Further tests with combined radial and axial heat removal, together with refined analytical modelling, should allow the origin of the instabilities to be identified and agreement between theory and experiment to be improved.

ACKNOWLEDGMENT

31. The authors are indebted to Mr. G. Basque (CEN Grenoble) for guidance and assistance in making BACCHUS-T calculations and to Drs. J.M. Seiler (CEN Grenoble) and R. Webster (NPDE Dounreay) for their advice and support.

REFERENCES

1. WEBSTER R. Free-convection cooling of blocked fuel subassemblies in pool-type liquid metal fast reactors. Nucl. Energy, 1981, vol. 20, December, 481-493.

2. von WEISSENFLUH T. Probes for local velocity and temperature measurements in liquid metal flow. Int. J. Heat Mass Transfer, 1985, vol. 28, no. 8, 1563-1574.

3. DURY T.V. et al. Radial heat removal from the SONACO sodium-cooled rod bundle compared with BACCHUS-T and INCA computer predictions. Proc. 3rd Int. Top. Meeting on Reactor Therm. Hyd., Newport, 1985, October, Paper 17.F.

4. BASQUE G. et al. BACCHUS: A numerical approach to two-phase flow in a rod bundle. Nuc. Eng. Des., 1984, vol. 82, October, 191-204.

5. WEBSTER R. A three-dimensional thermal hydraulic analysis of the PFR steam generators. 1st UK Nat. Ht. Tr. Conf., IChemE Symp. Series No. 86, 1984, 241-258.

A generic study of the safety aspects of LMFBR roof covers under HCDA load conditions

B.L. SMITH, J.F. JAEGER, H.U. WENGER, C. INVERSINI

Federal Institute for Reactor Research, Würenlingen, Switzerland

The response of an LMFBR roof cover to HCDA loadings is examined using a combined 2D/3D modelling approach. A generic 3D roof design of box-type construction is adopted and analysis under specimen loads carried out using the finite element program ADINA. The reactor tank and all internal components below roof level are assumed axisymmetric with the containment code SEURBNUK-EURDYN employed to follow the accident progression. An interface between SEURBNUK-EURDYN and ADINA is provided via a 2D simulant roof model, chosen to match the principal response characteristics of the 3D roof, to enable any interaction effects occurring during impact to be assessed.

INTRODUCTION

1. The roof of a pool-type LMFBR performs an essential component support function and, together with the main vessel, forms part of the primary containment closure. During an HCDA the roof structure is subjected to large forces and its mechanical response, with particular regard to the prevention of leakage of radioactive material to the environment, is an important component in the assessment of overall containment integrity. Of particular concern is the possibility of direct pressure loading on the roof as a result of the impact from below of an accelerated coolant slug.

2. Detailed analysis of roof response is best undertaken using an appropriate structural code with 3D capability. Finite element programs such as ADINA [1], MSC/NASTRAN [2], ABAQUS [3], preferably backed up by computed aided graphics software such as UNISTRUC [4], provide the modelling sophistication necessary for the task. In addition, a number of hydrodynamics codes have been developed [5] to estimate HCDA roof loads, and to help in the general assessment of containment strength below roof level. These codes are very complex, usually restricted to 2D axisymmetric geometry, and require extensive validation programmes [6] to ensure reliability.

3. Traditionally, roof loading and reponse analyses have been decoupled, a strategy strictly valid only if roof response times are long compared to the load times, but is otherwise adopted for convenience. Roof loads, via structural load paths and by direct coolant impact, are first estimated under rigid roof assumptions, and then detailed study of the roof response is undertaken independently.

4. However, the roof is a very massive structure and could absorb considerable energy during the period of the load transient, mitigating damage effects elsewhere in the containment. A generic study of the interaction effects is reported in this paper. A particular feature of the work is the interfacing between the 2D axisymmetric reactor description adopted below roof level and the 3D roof representation. This is provided via a 2D simulant roof model, chosen to match the non-linear response behaviour of the 3D roof, and enables any interaction effects occurring during loading to be assessed. The principal analysis tools adopted for the study are the structural code ADINA [1], for the 3D and 2D roof modelling, and the containment code SEURBNUK-EURDYN [7], to follow the fluid structure interactions.

3D ROOF MODEL

5. Since we aim to estimate the energy absorbing capacity of a typical LMFBR roof structure, and its influence on overall containment integrity, we adopt a roof model sufficiently realistic to be representative of current design thinking but at the same time avoiding, as far as possible, design specific details. The model chosen is shown in Figure 1.

6. The central plug is assumed stiff while the annular portion is a box like structure of plate steel made up of top and bottom facing plates, radial shear webs, inner and outer rings, and a cylindrical support skirt. A ring of steel-lined holes of equal radius is used to represent the major roof penetrations for the pumps and IHX's. All plates are of 50 mm thickness and modelled using triangular 3D plate elements from the ADINA library. The box is completely filled with concrete modelled as 4 layers of 8-cornered solid elements matching the steel mesh. Because of mirror symmetry, only a sector of the roof annulus is modelled explicitly.

7. The coupling between the central plug (which incorporates the various rotating shields) and the inner ring of the roof is assumed unable to withstand bending forces and a simple hinge connection is used. All other steel connections are stiff to simulate welds. The assumption is made that no shear forces are transferred between the steel plates and the concrete in-fill and that the steel can slide on the concrete surface but cannot separate from

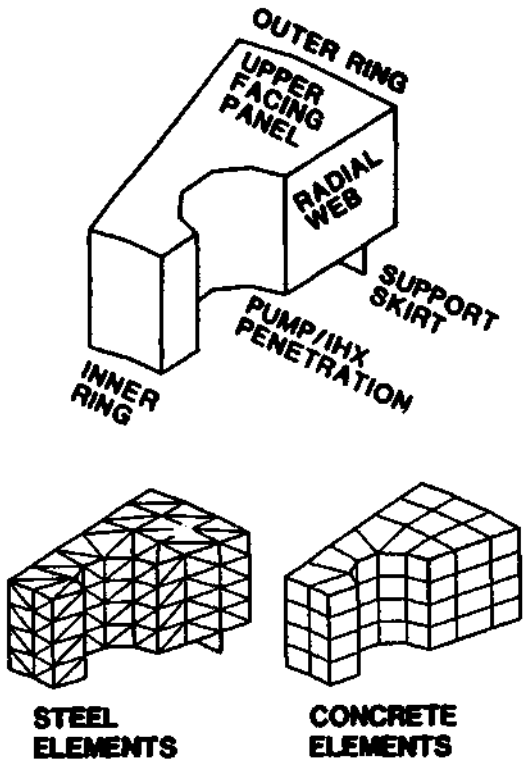

Figure 1 : ADINA Roof Model (3D)

it. The model is artificially stiffened by constraining some nodes to move together and spreading applied forces to avoid local stress concentrations which detailed design would eliminate. Further details of the model are given in References [8],[9].

2D REACTOR MODEL

8. A 2D axisymmetric representation is adopted for the reactor tank and for all internal components below roof level, Figure 2. Dimensions are appropriate for a commercial plant of 1300 MW(e) capacity.

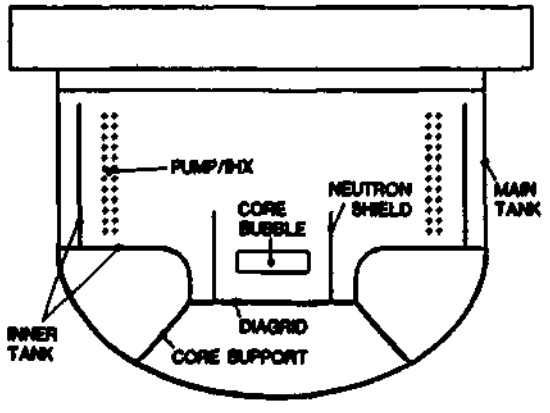

Figure 2 : Reactor Calculation (Rigid Roof)

9. The primary tank is cylindrical with a curved base and encloses the core and support structures, an inner tank separating the hot and cold sodium pools, as well as the pumps and IHX's. The core support assembly bears on the base of the main vessel to which it transmits loads resulting from the core pressurisation. The vessel in turn transmits the loads to the roof structure at its upper rim.

10. Many of the simplified structures seen in Figure 2 are composites of actual design features, and masses and strengths are enhanced accordingly. Thus, for example, the diagrid assembly includes a mass contribution arising from the core remnants, principally the radial and axial breeder zones. The neutron shield assembly has mass corresponding to the outer radial shield reflectors but strength compatible with a thin outer restraining barrel. The main tank has modified material properties to take account of the presence of nearby structures: the curved section above the junction with the diagrid support includes the mass and strength of the lower internal baffles, while the section below the junction incorporates the structural enhancement due to an attached core-catcher device.

11. The above core structure is assumed sufficiently weak for its effects on the flow dynamics to be ignored. The ring of IHX's and pumps, which experiments indicate do not produce strong asymmetries under HCDA conditions [10], is represented in a simplified way in which the blockage effect is taken into account by use of an annulus of porous material.

12. The energy source is provided by an expanding gas bubble of initial volume matching that of the inner fissile region of the core, and represents a work capacity of 1/2 GJ for an expansion to the cover gas volume.

13. In the finite element representation of the reactor model using SEURBNUK-EURDYN, all internal components are assembled using thin shell elements (not discernible in Figure 2). These may be generated automatically within the code and avoid unnecessary data preparation for those aspects of the problem not related directly to the calculation of the roof loads.

RIGID ROOF REACTOR CALCULATION

14. In the first instance we compute rigid roof loadings for input to the 3D ADINA roof model. Figure 3 shows the reactor configuration 115 msec into the transient, as calculated by SEURBNUK-EURDYN.

15. The bubble is seen to have expanded out of the core barrel, this having deformed considerably. The accelerated sodium slug above the bubble impacts the roof at 60 msec on the axis of symmetry. The impact zone spreads along the roof radius compressing the cover gas into the upper extremities of the vessel causing straining.

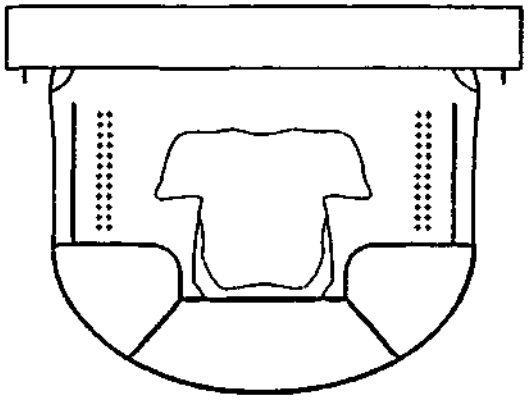

Figure 3 : Rigid Roof Calculation (t=115 msec)

16. The calculation was continued to 210 msec with the roof load histories given in Figure 4. At the start of the transient the core bubble pressure is high and the pressure differential across the diagrid is transmitted via connecting structures to produce a line load on the roof at the junction with the main tank; force 6 in Figure 4. This "pull-down" force peaks early at 6 MN/m due to plastic yielding of the tank. This value should be compared with the dead-weight load of 1 MN/m.

17. The second loading event occurs as a consequence of the slug impact, the roof loading being in the form of a pressure pulse of some 60 msec duration followed by a gradual pressurisation as the system approaches equilibrium. Pressures are displayed for five different radial locations in Figure 4. Peak pressures occur at progressively later times along the roof radius as the impact zone develops.

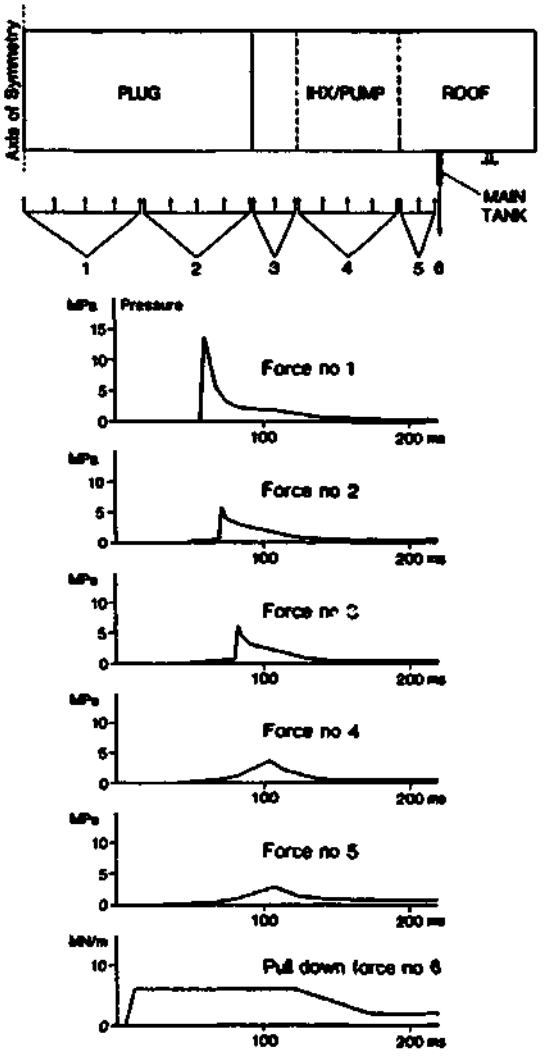

Figure 4 : Calculated Roof Loads

3D ROOF CALCULATION

18. The dynamic response of the 3D roof and plug assembly has been carried out using ADINA for the load functions given in Figure 4. The pull-down force transmitted by the main tank is applied across the roof thickness at the radius indicated in the Figure. The pressure distribution is assumed uniform at the five different areas of the bottom plate corresponding to the locations of the calculated slug pressure.

19. For the plug, which is not included in the finite element model, the resultant force is simulated by an appropriate line load applied to the inner ring of the roof annulus. Similar line loads have been used for the cylindrical area of the pump/IHX penetrations. Further details of the model are given in References [8],[9].

20. Both linear and non-linear analyses have been performed. In the non-linear regime the steel material response is assumed elastic-plastic with a yield criterion similar to von Mises, while ADINA's Drucker-Prager material model is used for the concrete with a tension cut-off and a cap on the compression strength, [8].

21. The results show that the roof structure is able to withstand the effects of the pull-down force within the linear range, but shortly after roof impact a wave of plasticity propagates from the inner ring along the vertical shear webs to the support skirt, Figure 5. There is some yielding of the top plate, indicated in the Figure, but the bottom plate remains unyielded throughout the loading period due to the high compression strength of the concrete above. Some non-linear behaviour for the concrete (cracking) is also observed.

22. For both the linear and non-linear cases very little lateral tipping of the model takes place (a few percents) and the global roof motion appears to be dominated by the fundamental radial mode.

2D EQUIVALENT ROOF MODEL

23. The absence of genuine 3D motions and the basic modal behaviour of the roof encourages us to look for a simple equivalent structure in the form of a homogeneous plate with modified material properties. For a plate of the correct

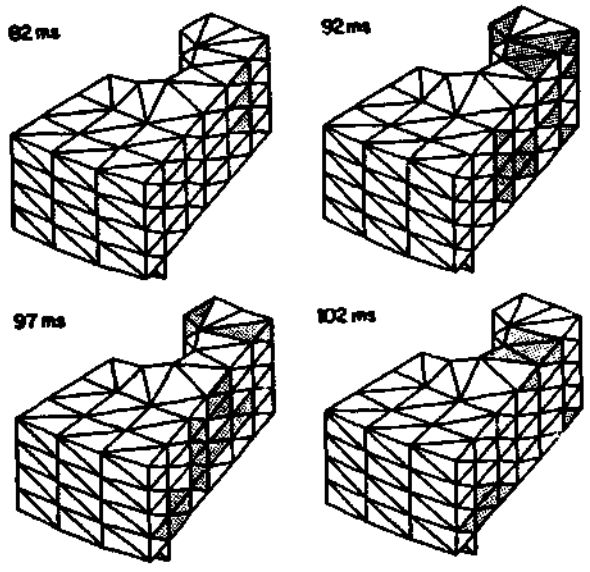

Figure 5 : Progress of Plasticity Wave

radial dimensions and of height h, the elastic lateral behaviour will be characterised by the two parameters ρh and Eh^3, representing inertia and flexural rigidity, respectively. The equivalent density ρ is chosen to preserve total mass while the equivalent Young's modulus E may be determined by matching static deflections or periods of free vibration. Fitting the vibration period proves to be more important as it will govern the whole time behaviour including the elastic recovery for the non-linear case. This will leave some error in the peak dynamic deflections.

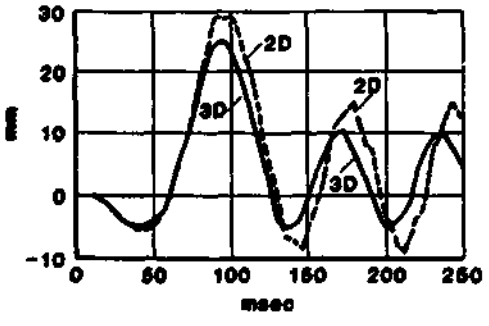

Figure 6 : Matching of Plug Displacements (Linear Model)

24. Plug displacement histories for the optimum linear 2D equivalence model are compared with those for the 3D model in Figure 6. In order to decouple the roof response from any effects due to the support skirt, the skirt was replaced by a simple support for these calculations. The load functions are those given in Figure 4 in both cases.

25. The initial dip in the plug deflection is due to the action of the pull-down force but the subsequent rise is accelerated by slug impact on the plug beginning at 60 msec. The period of free oscillation of the plug-roof assembly is 55 msec which is comparable to the pulse width of the loading function (see Figure 4). Results are given for a hinged coupling between the plug and the roof annulus, but the equivalence model proves to be sensibly independent of the coupling condition, [9]. The Young's modulus for the equivalent roof structure turns out to be very close to that used for the concrete in the 3D model indicative of the influence of the concrete stiffness on the total roof strength in the linear case.

26. When setting up the non-linear equivalence two further parameters become available: the yield strength σ_y of the material and the strain hardening slope E_1. The plug deflections for the 3D and 2D models are compared in Figure 7 for the best choice elastic/perfectly-plastic material (E_1=0); the yield strength σ_y being chosen to match the peak deflection.

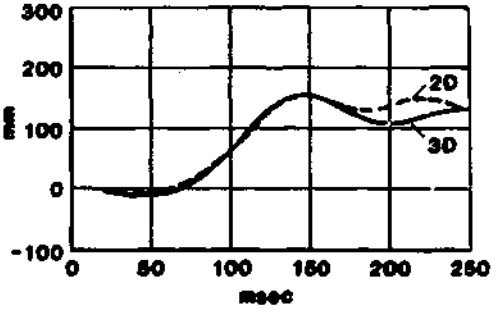

Figure 7 : Matching of Plug Displacements (Non-Linear Model)

27. The fit is not as close as in the linear case, particularly at later times, but there is no option to change the Young's modulus as the rise to the peak already occurs correctly. The final permanent offset however, is good. Note the factor 6 increase in peak deflection for the non-linear model.

28. The introduction of up to 4% strain hardening has very little effect on the results implying that the residual strength of the structure comes from the unyielded sections rather than work hardening effects elsewhere. The equivalence model in the non-linear case is more sensitive to the condition adopted for the plug-roof coupling than for the linear case. Full details are presented in Reference [9].

FLEXIBLE ROOF REACTOR CALCULATION

29. Refinement of the 2D equivalence model will mean a departure from the simple homogeneous plate to a more complex heterogeneous structure. In our case this is unnecessary since the divergence from the 3D results occurs after 170 msec (see Fig. 7) when the impact

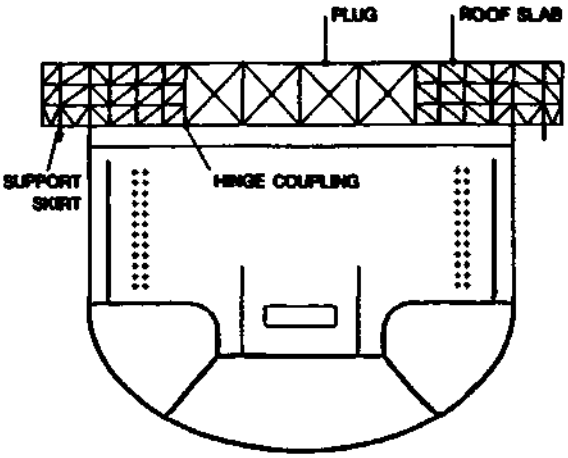

Figure 8 : Reactor Calculation (Flex Roof)

loading is complete. We can therefore examine the fluid-structure interaction effects occurring during the loading period using the existing model.

30. The flexible roof reactor configuration is given in Figure 8. Below roof level the arrangement is as before for the rigid roof case, but the roof and plug are now modelled explicitly using axisymmetric triangular elements from the EURDYN library, and the support skirt, made up of shell elements, is also included.

31. The SEURBNUK-EURDYN calculation was carried to 200 msec. The chronology of events before roof impact is almost identical with the rigid roof calculation. The downward displacement of the plug due to the action of the pull-down force peaks at about 40 msec and then there is partial elastic recovery before slug impact occurs at the plug centre at 60 msec. The high impact pressures further accelerate the roof assembly producing a peak plug displacement of 96 mm at t=160 msec. A sketch of the plug-roof coupling at maximum strain is given in Figure 9.

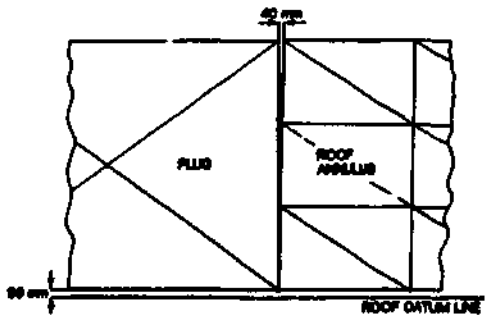

Figure 9 : Maximum Plug-Roof Separation

32. The principal post-loading event is the straining of the upper cylindrical portion of the main tank, occurring first near the junction with the roof but then spreading downwards. The reactor configuration at the final step in the calculation is shown in Figure 10 corresponding to a maximum bubble work of 550 MJ.

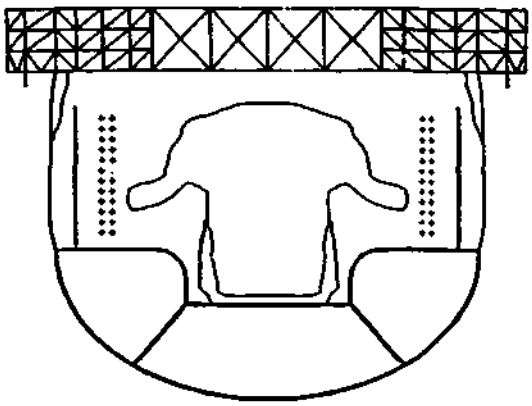

Figure 10 : Flex Roof Calculation (t=200 msec)

FINAL REMARKS

33. It has been shown that under the dynamic loads expected with HCDA phenomena it is possible, for the purposes of fluid-structure containment analyses, to represent the roof of a pool-type LMFBR with an axisymmetric model despite actual 3D design features due to penetrations, radial webs, the sandwiching of concrete in steel, and despite non-linear material behaviour. This is due to the lateral rigidity of the structure which limits azimuthal variations, and the dominance of the radial fundamental mode during loading. It has been demonstrated that a homogeneous plate with simple non-linear material properties is sufficient to match the principal response characteristics of the roof model adopted in this study. There appears to be little need for a more complex model.

34. Equivalent material properties are found by comparing 2D and 3D responses:
(1) Density is chosen to preserve mass;
(2) Young's modulus is adjusted to match the period of the linear responses, (the value found is close to that used for the concrete demonstrating the influence of the concrete stiffness on the linear motion);
(3) Material yield strength is chosen to match the amplitude of the non-linear response, (no strain hardening).

35. Concerning overall containment behaviour, the following observations can be made:
The roof model appears to be realistic, the maximum roof deflection (96 mm for a mechanical energy release of 550 MJ) calculated using the equivalent roof model, when appropriately scaled, agrees well with the deflection measured in the MARS experiment [11], a 1/20th scale mock-up test performed in France in support of the Superphenix safety analysis. The maximum

horizontal separation between the plug and roof upper surfaces, 40 mm in Figure 9, may have some consequences for some plug retention designs involving shear key arrangements. More detailed modelling of the plug-roof coupliug system is here indicated.

36. As remarked earlier, the transmission of the pull-down force to the roof early in the transient is limited by axial yielding of the main tank, which in our case has thickness 25 mm and is the only load bearing structure in contact with the roof, see Fig. 4. The transfer of the shear load to the support skirt, and hence to the reactor vault, via the radial web network is accomodated within the linear range of the steel. If however, there are additional load paths to the roof via inner tanks, baffles or pump shrouds, much larger forces may be transferred and the integrity of the roof structure under shear loads may need closer examination.

37. Due to the large strength and inertia of the plug-roof assembly, taking account of roof flexibility leads to only marginal reduction in the total roof load (2.5%) compared to the rigid roof case. This result implies that it is feasible to perform detailed structural analyses of the roof in isolation from the rest of the containment using rigid roof loadings:- the de-coupled approsch.

38. However, in the overall assessment of containment strength, and mechanical damage to structures below roof level, it is necessary to include the effects of roof flexibility. Figure 11 compares hoop strain histories for the cylindrical section of the main tank for the flexible and rigid roof calculations. The reduced final strain for the flexible roof case illustrates the significant energy absorbing capacity of the roof, even for modest roof displacements.

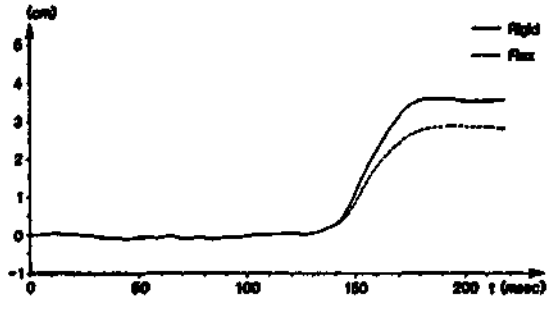

Figure 11 : Upper Vessel Hoop Strains

39. Thus results from the work completed so far show that in HCDA safety analyses detailed assessment of the strength of the roof structure can proceed adequately using rigid roof loads, but in the general assessment of containment integrity for weaker structures below roof level, account must be taken of the energy absorption due to roof movement in order to reduce conservatism.

REFERENCES

1. "ADINA - A Finite Element Program for Automatic Dynamic Incremental Nonlinear Analysis". ADINA Engineering Report AE 81-1, Watertown, MA (Sept. 1981).

2. McCORMICK,C.W. "MSC/NASTRAN - User's Manual" MacNeal-Schwendler Corp., California (1978).

3. HIBBITT,H.D. "ABAQUS/EPGEN - A General Purpose Finite Element Code with Emphasis on Non-Linear Applications", Nucl.Eng.Des., 77, 271 (1984).

4. UNISTRUC, Control Data Corporation, Minneapolis, Minnesota (1978).

5. CHANG,Y.W. "Analysis of HCDA", Nucl.Eng. Des., 69, 345 (1982).

6. ALBERTINI,C. et al "The JRC-COVA Programme, Final Report", EURATOM Report EUR 8705 EN (1983).

7. SMITH,B.L. "A New Fluid-Structure Coupling Algorithm for the LMFBR Containment Code SEURBNUK-EURDYN", Paper B2/6, SMIRT-8, Brussels (Aug 1985).

8. SAURER,G. et al "Dynamic Response of an LMFBR Deck Structure Under Slug Impact", Computers & Structures, 21, 159 (1985).

9. JAEGER,J.P. et al "Modelling of an LMFBR Cover for Fluid-Structure Interaction Studies", Paper E7/7, SMIRT-8, Brussels (Aug 1985).

10. BRASSINDALE,J.A. et al "Three Dimensional Aspects of Fast Reactor Containment Loading Studies", Paper E1/1, SMIRT-7, Chicago (Aug 1983).

11. PALGAYRETTES,M. et al "Response of a 1/20 Scale Mock-Up of the SUPER-PHENIX Breeder Reactor to an HCDA Loading Simulation", Paper E4/1, SMIRT-7, Chicago (Aug 1983).

The origin and magnitude of pressures in fuel coolant interactions

W. HEER, D. JAKEMAN, B.L. SMITH

Federal Institute for Reactor Research, Würenlingen, Switzerland

A number of small scale experiments to simulate fuel coolant interaction (FCI) effects have been carried out using Freon and water. Contrary to the predictions of most current FCI models, only modest pressure transients are observed within the interaction region itself but large pressure spikes, near to or above critical Freon pressure, are seen at the boundaries of the region. Similar pressure amplification effects have been noticed in parallel experiments involving two phase mixtures. It is suggested that in both cases a water hammer type effect is the cause of the pressure spikes. These observations could form the basis of new thinking in FCI modelling.

INTRODUCTION

1. In spite of the attention paid to fuel coolant interactions (FCI's) and the consequences of them in fast reactor safety philosophy, the underlying physical principles of the interaction are still not fully inderstood. An examination of some aspects of the problem has been carried out in simple geometries in the context of a number of small scale experiments. Particular attention is paid to the origin of high pressures commonly associated with FCI's.

INTERACTIONS WITH FREON AND WATER

2. To study the behaviour of FCIs, Freon, simulating the coolant, is poured into a narrow tube partially filled with water at 80 °C simulating the molten fuel. The type of Freon used is $ClCHF_2$ (boiling point: -40.8 °C, crit. temperature: 96 °C, crit. pressure: 4.9 MPa). A square aluminium tube (inner width: 3 cm) is used but square Perspex tubes are also employed to give an additional visual display. Pressure transients are measured at various locations along the length of the tube by piezo-electric pressure transducers (Kistler 6031 or 603B) and recorded by a 12 channel memory transient recorder. To facilitate interpretation, flash photographs are taken and, for selected tests, high speed cine photography (5000 f/s) is also used.

3. Out of 110 tests carried out 91 tests produced a significant interaction. Common to all tests is the appearance of a quasi-stable premixing zone of several cm length at the upper end of the water column. The zone remains in a churning state for about ½ s before the interaction spontaneously starts and rapidly spreads over the entire premixing zone. Although every test shows individual features in its pressure trace there is nevertheless surprisingly good consistency between groups of tests selected according to where the interaction started. Two types may be identified, those in which the interaction started near the bottom of the interaction region (type 1) and those in which the interaction started near the top (type 2). Fig. 1 shows a typical set of pressure traces for each type. Some 17 % of the interactions were of type 1, 37 % of type 2. In the remaining tests the interactions started at an intermediate point, and in these cases type 1 behaviour was observed above the starting point and type 2 behaviour below. Type 1 interactions propagate upwards with an average velocity of 120±50 m/s (min. 60 m/s) and a pressure pulse of average size 0.7±0.2 MPa (min. 0.35 MPa, max. 1.0 MPa). Type 2 interactions, propagating downwards, have essentially the same behaviour within the interaction region itself (average velocity: 150±80 m/s, min. velocity: 50 m/s, average pressure 0.7±0.2 MPa) but as soon as the pressure waves reach the lowest transducer positions (< 60 mm) high pressure spikes up to 6 MPa are observed. Photographs taken at various times during the interaction indicate the passage of the wave front. Fig. 2 is a good example in which a type 2 interaction started near to pos.4 and had reached pos.2 when the flash lamp was triggered. The interaction propagates down to pos.1 where the large pressure spike is produced. The Figure shows also a reflected wave similar in amplitude and velocity to the initial wave and superimposed on it. This behaviour is associated with the bottom edge of the interaction region lying between pos.1 and 2. The Freon seen in the photograph below pos.1 did not react in this case. Below the interaction region the pressure spike is transmitted through the water and is itself reflected at the bottom of the tube. The separation of the downward and reflected peaks at pos.1 suggests a velocity of about 1000 m/s, well in excess of the propagation speeds within the interaction region above. The pressure traces further indicate that only 30 % of the peak heights at pos.1 are due to superposition.

4. The generation of pressure spikes can be explained in the following way. Pressure waves passing through the essentially two phase interaction region accelerate (and compress) the

fluid behind the wave front. It is the stopping of this fluid when the waves reach the relatively incompressible boundary of the interaction region which creates the high pressure by a type of water hammer effect. We show later how pressures of 6 MPa amplitude may be produced in such circumstances, providing there is significant condensation of material accompanying the compression immediately behind the wave front (see Paragraph 8). Pressures would be expected to propagate both forwards into the incompressible region and backwards through the now compressed material behind the wave front. This picture is consistent with the observations. However, the pressure of the reflected wave is much reduced below the hammer pressure and its velocity is much smaller than the single phase velocity. This suggests there can only be a small region behind the wave front in which vapour remains condensed, the two phase state quickly re-establishing itself (because of the vapour production by the interaction). There is evidence of a rapid local variation of 10 μs duration superimposed on the pressure spike which can be seen on the traces for an enlarged time scale, Fig.3. This could be caused by the collapse of individual vapour pockets.

PRESSURE WAVES IN AIR-WATER MIXTURES

5. In order to pursue our explanation of the observed pressure spikes in analytical terms a simple theoretical model of the water hammer process is formulated and tested against measured values.

Theoretical model

6. The model describes a pressure wave passing through an air-water mixture being partially reflected as well as transmitted at an interface to a less compressible region. One-dimensional geometry is used. The ideas are displayed in Fig.4 and the explanation of the symbols is given below:

P_i = pressure (P_o = 0.1 MPa)

v_{xi} = specific volume of air (x=a) and water (x=w) relative to the mass of the mixture

$v_i = v_{ai} + v_{wi}$ = specific volume of the mixture

$\alpha_o = v_{ao}/v_o$ = volume fraction of air at P_o

$\rho_i = 1/v_i$ = density of the mixture

ρ_{ao} = 1.2 kg/m^3 density of air at P_o

ρ_{wo} = 1000 kg/m^3 density of water at P_o

κ_{ij} = mean compressibility of the mixture

β = 4.6 E-10 Pa^{-1}, compressibility of water

γ = 1.4, isentropic exponent of air

U_{ij} = wave velocity (Pressure step: $P_j - P_i$)

V_i = fluid velocity behind the wave front

7. An approximation for the equation of state is obtained by assuming isentropic compression for the air component and constant compressibility for the water. This leads to the following relations for a pressure change from P_o to P_i:

$$(v_{ai}/v_{ao}) = (P_o/P_i)^{\frac{1}{\gamma}} \quad \text{air} \qquad (1)$$

$$(v_{wi}/v_{wo}) = \exp[-\beta(P_i-P_o)] \approx 1-\beta(P_i-P_o) \quad \text{water} \qquad (2)$$

$$(v_i/v_o) = \alpha_o(v_{ai}/v_{ao}) + (1-\alpha_o)(v_{wi}/v_{wo}) \quad \text{mix} \qquad (3)$$

where

$$v_o = 1/(\alpha_o\rho_{ao} + (1-\alpha_o)\rho_{wo}) \qquad (4)$$

is the inital specific volume of the mixture.

Conservation of mass and momentum for the incident wave (see Fig.4) can be expressed as

$$U_{o1}/v_o = (U_{o1}-V_1)/v_1 \qquad (5)$$

$$P_1-P_o = U_{o1}^2/v_o - (U_{o1}-V_1)^2/v_1 \qquad (6)$$

which enable U_{10}, V_1 to be determined for a given pressure step (P_1-P_o). Defining a mean compressibility κ_{ij} for compression from P_i to P_j by:

$$\kappa_{ij} = (-1/v_i)(v_j-v_i)/(P_j-P_i) \qquad (7)$$

we have, using (2), (3),

$$\kappa_{ij} = \frac{v_o}{v_i}\left(\alpha_o \frac{\frac{v_{ai}}{v_{ao}} - \frac{v_{aj}}{v_{ao}}}{P_j - P_i} + (1-\alpha_o)\beta\right) \qquad (8)$$

hence for the initial wave we obtain:

$$U_{o1} = 1/\sqrt{\kappa_{o1}\rho_o} \quad \text{wave velocity} \qquad (9)$$

$$V_1 = \sqrt{\kappa_{o1}/\rho_o}\,(P_1-P_o) \quad \text{fluid velocity} \qquad (10)$$

For pure materials ($\alpha_o \to 0$, $\alpha_o \to 1$) and small pressure pulses ($\beta(P_1-P_o) \ll 1$, $(P_1-P_o)/P_o \ll 1$), Eq.(9) is identical with the well known expressions for velocity of sound in water and air ($U_{10} = 1/\sqrt{\beta\rho_{wo}}$, $U_{10} = \sqrt{\gamma P_o/\rho_{ao}}$). With increasing air fraction U_{10} decreases rapidly, goes through a shallow minimum at $\alpha_o = 0.5$, but then increases steeply as α_o approaches 1. Typical values at the minimum are 24 m/s for $(P_1-P_o) < 0.0001$ MPa and 95 m/s for $(P_1-P_o) = 2$ MPa.

8. The wave and fluid velocities U'_{02}, V'_1 for the transmitted wave are obtained from Equations analogous to (8)-(10) but with the pressure step P_2-P_o (cf. Fig.4). Taking into account the fact that the reflected wave travels in a fluid moving with velocity V_1 towards the wave front, we obtain correspondingly to Eq. (9)-(10):

$$U_{12} = (1/\sqrt{\kappa_{12}\rho_1}) - V_1 \quad \text{wave velocity} \qquad (11)$$

$$V_2 = V_1 - \sqrt{\kappa_{12}/\rho_1}\,(P_2-P_1) \quad \text{fluid velocity} \qquad (12)$$

With P_2 calculated from the interface condition $V_2 = V'_1$ (in most cases numerically) the velocities U_{12}, V_2 are determined. These results, which strictly refer only to the interface, are also applicable to a square wave for the duration of the pulse. The pressure magnification of the reflected wave may be written in terms of acoustic impedance as:

$$\frac{P_2-P_1}{P_1-P_o} = \frac{1/(\rho_o U_{o1}) - 1/(\rho_o U'_{o2})}{1/(\rho_1 U_{12}) + 1/(\rho_o U'_{o2})} \qquad (13)$$

The following comments can now be made:
- Pressure magnification is obtained only if the acoustic impedance of the reflected wave exceeds that of the incident wave.
- The influence of the factors involving primed variables, corresponding to the medium of the transmitted wave, decreases with the compressibility of the medium and is identically zero for a solid wall.
- Equation (13) remains valid for steam water mixtures where evaporation and condensation effects could take place, though Eq.(1) must be abandoned and a more appropriate equation of state used. Very large pressure amplifications are possible in this cases if complete condensation occurs as a result of the passage of the incident wave, $\rho_1 U_{12} >> \rho_o U_{10}$.
- Equation (13) can also be used to estimate the hammer pressures produced in the Freon experiments. Assuming full condensation behind the incident wave front and approximating compressibility and density of the mixture of water and liquid Freon by appropriate values for water, the equation simplifies to:

$$(P_2-P_1)/(P_1-P_o) \simeq (\rho'_o U'_{o2})/2(\rho_o U_{o1}) \qquad (14)$$

Inserting typical values, U_{10} = 150 m/s, (P_1-P_o) = 0.7 MPa, α_o = 0.3, ρ'_o = 1000 kg/m^3, U'_{o2} = 1470 m/s we obtain according to (14), (4) a pressure magnification: $(P_2-P_1)/(P_1-P_o)$ = 7 and a hammer pressure (P_2-P_o) = 6 MPa, in accordance with the remarks in Paragraph 3.
- Theoretical curves showing pressure and velocity magnifications for a range of parameters are given in Ref.1.

Experiments

9. The model is tested against experiments performed in air water mixtures using the same equipment as for the Freon experiments. The air is introduced at the base of the aluminium tube via a feed pipe. A pressure pulse is produced at the top of the tube using an accelerated wooden plug. Additional experiments in a Perspex tube have also been performed and these are reported in Ref.1.

10. Two examples of the measured pressure trace are shown in Fig.5. The first, test 515, is a calibration test in which a pressure pulse is propagated through pure water. A symmetric reflection at the base of the tube can be seen from the pressure traces. The second example, test 518, shows a reflection in an air-water mixture. The reflection is not symmetric in that case showing that some compression of the mixture has taken place. The velocities of the initial and the reflected waves are well defined and the corresponding pressure steps, although less accurate, can clearly be recognised. The second pressure step generated at the top of the tube appears to be assocoiatad with the plug motion. In Fig.6 the calculated initial wave velocity as a function of α_o is presented for different values of the pressure step (P_1-P_o). Because P_1-P_o is different for each experimental point the corresponding theoretical values are given by circles in the Figure. Experimental points are indicated by crosses. Agreement between the calculated and observed points appears adequate and illustrates the general behaviour of pulses travelling through a bubbly mixture. The reduction of velocities to values well below the sound velocities in either all water of all air is worth noting. In Fig.7-8 similar representations are given for velocity and pressure magnification. The measured values show that increases by factors of 2 to 3 are possible, and that small initial pressure waves can produce fairly large amplifications. The agreement of the experiment with the calculation shows that the model is able to describe the main features of the observed behaviour. Perfect agreement is not to be expected because the shape of the incomming pressure wave is not square, as required by the analytical model, and the air bubbles are not simply compressed but are fragmented by the initial pressure wave. This behaviour can be seen in Fig.9.

PRESSURE WAVES IN STEAM-WATER MIXTURES

11. To provide further information on the behaviour of pressure waves in two phase mixtures additional experiments have been performed using steam water mixtures. The test geometry is similar to before. Pressure transients of selected tests with progressively increasing steam content are shown in Fig.10. The velocity of the downcomming wave decreases with increasing steam content and the corresponding pressure profile flattens and lengthens. The amplitude of the reflected wave is very noticeable and several times larger than that of the incident wave. In the last test, with 10 % steam content, the incident wave cannot be discerned above the background noise, but the reflected wave is very pronounced. The velocity of the reflected wave approaches the velocity of sound in water indicating an almost complete condensation of all the steam behind the incident wave front. Furthermore, velocity and amplitude are maintained to the top of the tube showing that the vapour does not re-establish itself. This pattern is in contrast to the experiments with Freon in which velocities and pressures of the reflected wave almost immediately return to values similar to those of the incident wave. Returning to Fig.10, at the top of the tube a rarefaction wave is generated and this invariably propagates downwards at the velocity of sound in water. Although a full analysis is not performed in this case a consistency test has been made. The parameters of the incident wave and the pressure magnification obtained by two different methods are given in Table 1. The magnifications derived directly from pressure traces in Fig.10 are given in column "measured". These show a magnification which increase from 3 to 10 with increasing steam fraction. For reflection at a solid wall, appropriate in this case, Eq.(13) simplifies to:

$$(P_2-P_1)/(P_1-P_o) = \rho_1 U_{12}/\rho_o U_{10} \qquad (15)$$

The velocities U_{10}, U_{12} can also be determined directly from the pressure traces in Fig.10. The

ratio ρ_1/ρ_o of the densities calculated according to Eq.(3) (with the assumption of full condensation) is close to unity in our cases. Pressure magnifications deduced from the velocities according to Eq.(15) are entered in column "deduced" of Table 1. The agreement indicates that the model is adequately describing the existing pressure-velocity relationships.

Table 1. Data of the pressure waves

α_o (%)	P_1-P_o (MPa)	U_{10} (m/s)	$(P_2-P_1)/P_1-P_o)$	
			measured	deduced
2	0.75	330	2.7	3.5
4	0.3	280	3.7	4.0
7	0.15	140	10	11

CONCLUSIONS AND COMMENTS

12. It is generally believed that the high pressures observed in FCI's, which can exceed critical coolant pressure, arise within the interaction region itself. To be able to explain these high pressures most of the FCI models assume some fragmentation mechanism and heat transfer by thermal conduction on the basis of liquid-liquid contact. Depending on the inertial confinement this is believed to give rise to high single phase pressure spikes within the interaction region. The experiments reported here are in contradiction to this picture. There is evidence instead that high FCI pressures are generated at the boundary of the interaction region by a type of water hammer effect and that within the region itself the pressures are more modest. Furthermore, indications are that the region contains vapour during all stages of the interaction. This suggests that models of FCI phenomena in which the presence of vapour plays a key role in the fragmentation and heat transfer processes seem more appropriate.

13. The conclusions being drawn from the present series of experiments need to be examined in the light of previous results from a much wider range of experiments. In the shock tube experiments in Ref.2 it seems probable that the interaction region is well below the pressure transducers which are all situated in a column of water having relatively low compressibility. It is believed that the observed pressures of up to 40 MPa arise from an upward travelling "hammer" pulse generated by an FCI at the bottom of the tube. The THERMIR experiments reported in Ref.3 are performed in a narrow tank geometry with transducers on the sides and thus would not be measuring the pressure within the interaction region itself. Although the transducers clearly show the passage of the interaction from one side of the tank to the other, the magnitude of the pressures are rather erratic. Perhaps the measurements are an integrated effect of the various hammer pressures arising from the complex geometry at the boundary of the interaction region. The experiments with Freon and water reported in Ref.4 are similar to those given here and show similar results including the high pressure spikes at the lower transducer position. We believe that the maximum pressures in these experiments, as with our own, are related to the geometrical arrangement rather than the heat transfer mechanisms taking place within the interaction region. This view appears to be consistent with those expressed in Ref.4 and also by the same authors in a more recent note (Ref.5).

REFERENCES

1. JAKEMAN D. et al. Propagation of pressure waves through air-bubble water mixtures. EIR-Bericht Nr. 534, 1984.
2. GUEST J.M. et al. Al/Water shock tube experiments at AWRE, Foulness. Paper SNI 2/1 Second specialist meeting on sodium/fuel interaction in fast reactors Ispra, 1973.
3. FRY C.J. and ROBINSON C.H. Results from selected experiments performed in the THERMIR facility at AEE Winfrith. AEEW-M 1778, 1980.
4. ANDERSON R.P. and ARMSTRONG D.R. R-22 Vapour explosions. Winter ASME Meeting, Atlanta 1977.
5. ANDERSON R.P., ARMSTRONG D.R. and BOVA L. Shock wave passage through two-phase mixtures, Trans ANS. 43, 509, 1982.

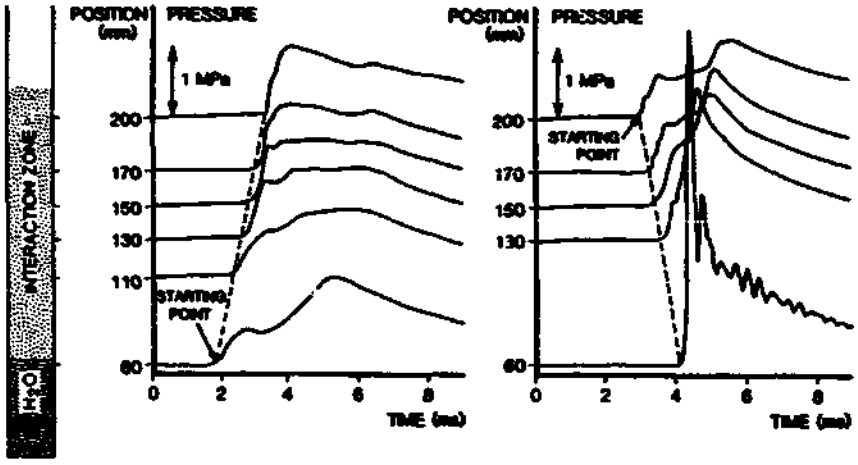

Fig.1 Pressure traces of interactions with different starting points

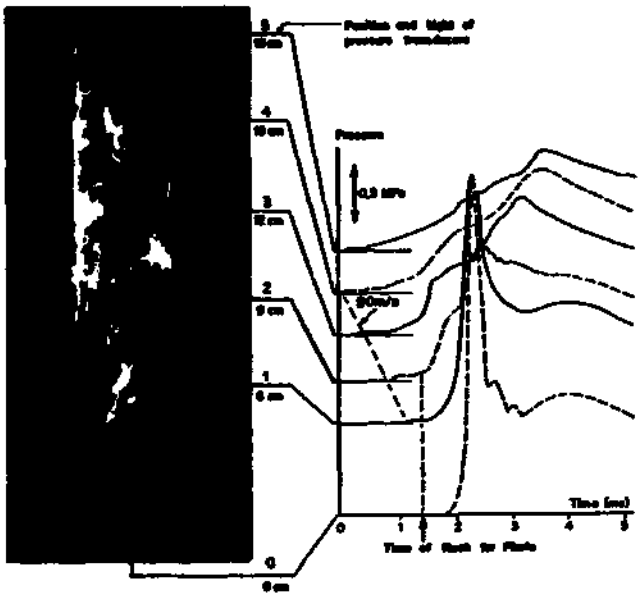

Fig.2 Relation of pressure traces to photo of interaction

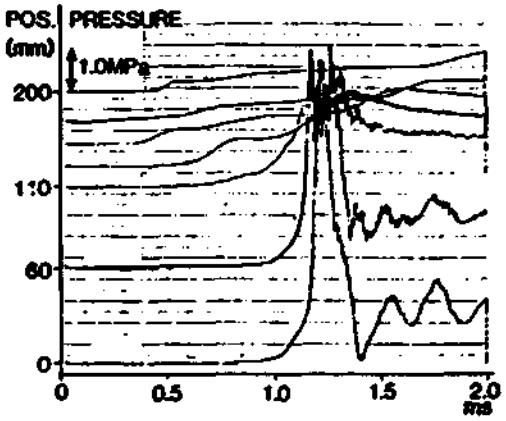

Fig.3 Details of pressure spike

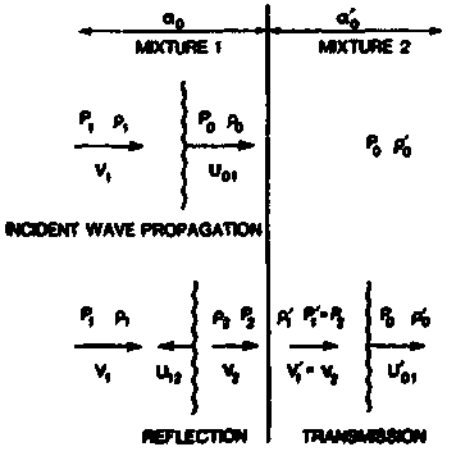

Fig.4 Notation used in the analysis

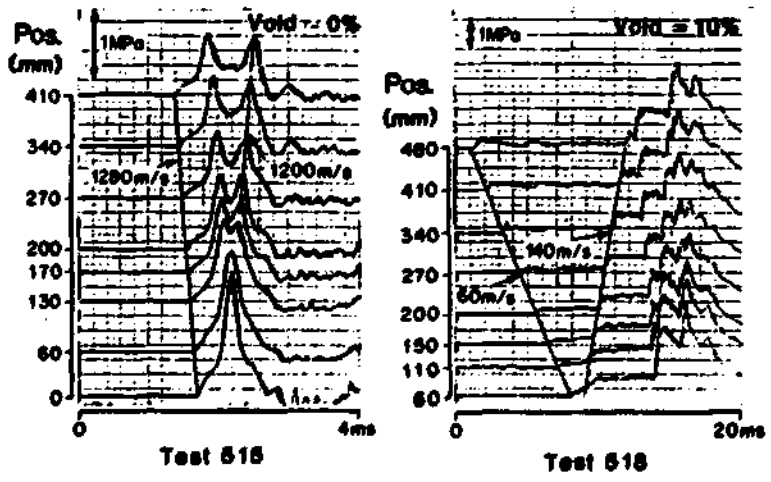

Fig.5 Pressure waves propagating through pure water and an air-water mixture

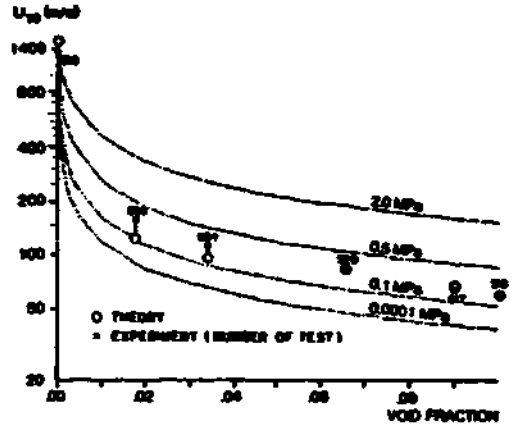

Fig.6 Wave velocities in air-water mixtures

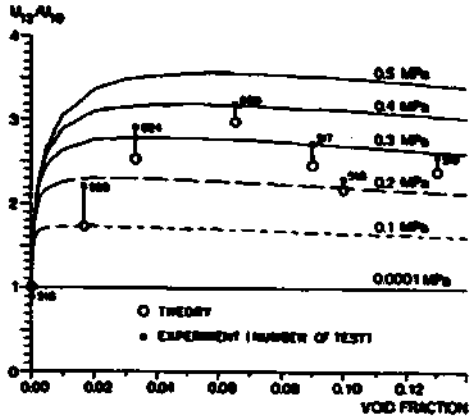

Fig.7 Velocity magnification in air-water mixtures

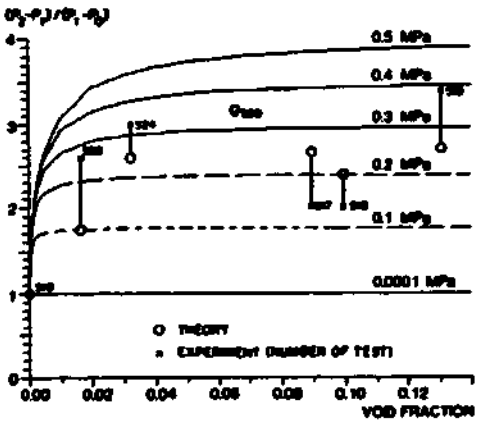

Fig.8 Pressure magnification in air-water mixtures

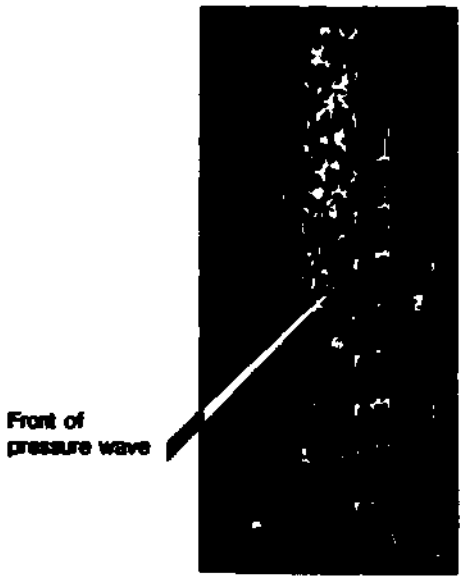

Fig.9 Photo of pressure wave in an air-water mixture

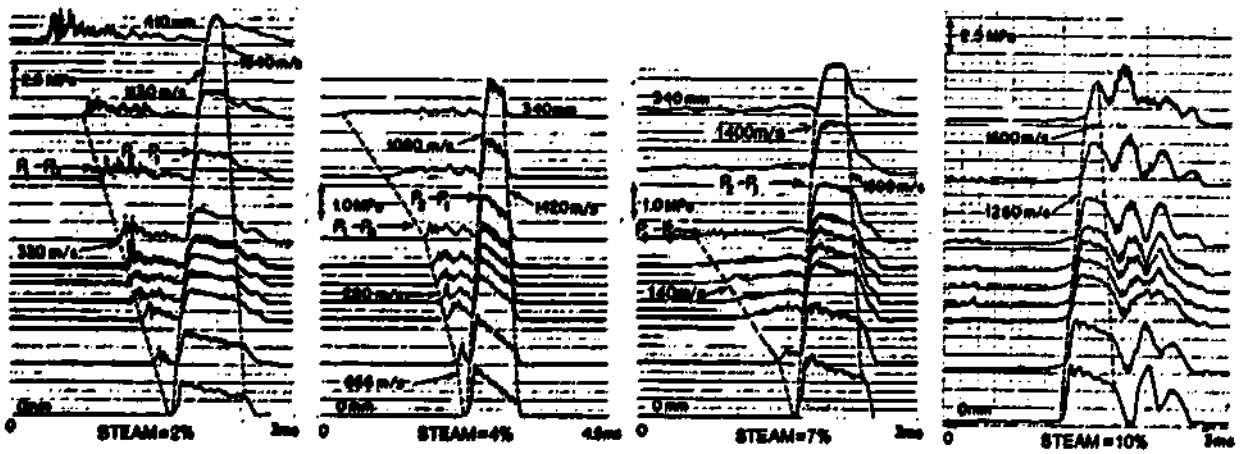

Fig.10 Pressure waves propagating through steam-water mixtures